



## Article

# Detection and Mapping of Active Landslides before Impoundment in the Baihetan Reservoir Area (China) Based on the Time-Series InSAR Method

Jiawei Dun <sup>1,2</sup>, Wenkai Feng <sup>1,2,\*</sup>, Xiaoyu Yi <sup>1,2</sup>, Guoqiang Zhang <sup>1,2</sup> and Mingtang Wu <sup>3</sup>

<sup>1</sup> State Key Laboratory of Geohazard Prevention and Geoenvironment Protection, Chengdu University of Technology, Chengdu 610059, China; djw@stu.cdut.edu.cn (J.D.); xiaou@stu.cdut.edu.cn (X.Y.); Zhangguoqiang@stu.cdut.edu.cn (G.Z.)

<sup>2</sup> College of Environment and Civil Engineering, Chengdu University of Technology, Chengdu 610059, China

<sup>3</sup> Zhejiang Huadong Construction Engineering Co., Ltd., Hangzhou 310000, China; wu\_mt@ecidi.com

\* Correspondence: fengwenkai@cdut.cn; Tel.: +86-028-84079301

**Abstract:** Many potential landslides occurred in the Baihetan reservoir area before impoundment. After impoundment, these landslides may still slide, affecting the safe operation of the reservoir area (e.g., causing barrier lakes and floods). Identifying the locations of landslides and their distribution pattern has attracted attention in China and globally. In addition, due to the rolling terrain of the reservoir area, synthetic aperture radar (SAR) imaging will affect the interactive synthetic aperture radar (InSAR) deformation results. Only by obtaining effective deformation information can active landslides be accurately identified. Therefore, the banks of the Hulukou Xiangbiling section of the Baihetan reservoir area before impoundment in the Jinsha River Basin were studied in this paper. Using terrain data and the satellite parameters from Sentinel-1A ascending and descending orbits and ALOS PALSAR ascending orbit, the line-of-sight visibility was quantitatively analyzed, and an analysis method was proposed. Based on the SAR data visibility analysis, the small baseline subset (SBAS) technique was used to process the SAR data to acquire effective deformation. InSAR deformation data was combined with Google Earth imagery to identify 25 active landslides. After field verification, 21 active landslides (14 new) were determined. Most of the active landslides are controlled by faults, and the strata of the other landslides are relatively weak. This InSAR analysis method based on SAR data visibility can provide a reference for identifying and analyzing active landslides in other complicated terrain.

**Keywords:** SBAS-InSAR; Baihetan reservoir area; visibility; active landslide; landslide identification



**Citation:** Dun, J.; Feng, W.; Yi, X.; Zhang, G.; Wu, M. Detection and Mapping of Active Landslides before Impoundment in the Baihetan Reservoir Area (China) Based on the Time-Series InSAR Method. *Remote Sens.* **2021**, *13*, 3213. <https://doi.org/10.3390/rs13163213>

Academic Editors: Andrea Manconi and Alessandro Cesare Mondini

Received: 1 July 2021

Accepted: 9 August 2021

Published: 13 August 2021

**Publisher's Note:** MDPI stays neutral with regard to jurisdictional claims in published maps and institutional affiliations.



**Copyright:** © 2021 by the authors. Licensee MDPI, Basel, Switzerland. This article is an open access article distributed under the terms and conditions of the Creative Commons Attribution (CC BY) license (<https://creativecommons.org/licenses/by/4.0/>).

## 1. Introduction

The Baihetan Hydropower Station is the second cascade power station developed in the lower mainstream of the Jinsha River and is currently the second-largest hydropower station in China. During development of the reservoir area, due to the long-term submersion, water level rise and fall, channel erosion, and wetting and drying cycles, the bank slopes slid and deformed to some degree [1–5]. The banks of the Baihetan reservoir area from Hulukou to Xiangbiling generate a strong tectonic force, which will result in high landslide risks after impoundment. This is a key reservoir segment of the Baihetan reservoir area where there are many residential areas, and thus, investigating the hidden dangers of landslides in this segment is very important. Therefore, there is an urgent need for an efficient and feasible method to determine the locations of landslides and analyze their distribution pattern.

The terrain conditions in the study are very complex, and extensive time and energy are required to monitor landslides with conventional methods. In addition, using these methods, it is difficult to identify disasters presenting as micro deformations. However,

the InSAR technique breaks through the limitations of conventional manual investigations and checks that cannot identify potential landslides from micro deformations, and it covers a wide range of areas and has advantages over conventional radar in both accuracy and resistance to weather interference [6–8]. Shi et al. [9] used Stamps InSAR technology to identify approximately 30 landslides in the area from Fengjie to Zigui in the middle of the Three Gorges Reservoir area after impoundment. Zhao et al. [10] identified 10 loess landslides in the Heifangtai area using InSAR technology. Dai et al. [11] detected 23 active landslides upstream and downstream in Zhouqu County using SBAS-InSAR technology, and selected relevant rainfall landslides for InSAR monitoring. The above research shows that it is highly feasible to use InSAR technology to identify regional landslides and monitor the deformation of a single landslide. The InSAR technique can be used for long-term deformation monitoring research on reservoir bank slopes. However, some unexamined problems remain in the above studies, and the influence on the InSAR monitoring results of the geometric distortion (layover, foreshortening, shadow, etc.) caused by the side-view imaging of the SAR system in the mountainous area has not been fully discussed.

Geometric distortions strongly impact the ability of SAR to monitor surface deformation, leading to observation failure and different deformation results for the ascending and descending orbits of the satellite [12–14]. When identifying regional landslide disasters, many researchers focus on the deformation monitoring results of InSAR technology, rarely considering the impact of geometric distortion on landslide disaster identification in mountainous areas [15–18], and rarely comparing or analyzing the identification results with field observation results [19–21]. To identify whether the target in the study area is within the line-of-sight (LOS) range of the radar and whether it can be fully expressed in a radar image, as well as the accuracy of the InSAR recognition results, visibility analysis and comparison of field observation results are very important [22]. To solve these problems, this paper analyzes the visibility of the study area before InSAR deformation monitoring, and a visibility analysis method is proposed to lay the foundation for obtaining effective deformation. The results of the final analysis are compared with field observation results.

Therefore, this paper uses ALOS PALSAR ascending orbit data and Sentinel-1A ascending and descending orbit data as data sources. First, quantitative analysis and discussion of the visibility of the SAR data of the Baihetan reservoir area from Hulukou to Xiangbiling are carried out in this paper. Because the SDFP points used by the SBAS method belong to distributed scatterer targets with strong coherence over a short time, they are more suitable for deformation monitoring of natural scenes such as mountain landslides [23,24]. Then, based on the visibility analysis, the SBAS-InSAR technique is applied to obtain information about the effective deformation, and the range of landslides is determined based on Google Earth images. Finally, the identification results are verified by a field investigation. According to the field investigation results, the development and distribution patterns of active landslides are analyzed. Our research will be beneficial to the prevention and early warning of landslides during and after the impoundment period of the Baihetan Reservoir, which will provide relevant references for the identification and analysis of regional active landslides under complex terrain in the future.

## 2. Study Area

The Baihetan Hydropower Station, located in Qiaojia County of Yunnan Province and Ningnan County of Sichuan Province, is 45 km from Qiaojia County (upstream), approximately 182 km from the Wudongde Hydropower Station (upstream), and 195 km from the Xiluodu Hydropower Station (downstream). The construction of the main station started in 2013, and the impoundment began in April 2021. The station will begin to generate electricity in July 2021 [23]. With a total capacity of 20.627 billion m<sup>3</sup>, the standard water level is 825.0 m. The flood control and dead storage levels are 785.0 m and 765.0 m, respectively.

The study area is in the Baihetan reservoir area from Hulukou to Xiangbiling, 50 km upstream to 10 km downstream of Qiaojia County, Yunnan Province, spanning five counties,

i.e., Qiaojia County, Huize County, Ningnan County, Huidong County, and Dongchuan District, with a total area of approximately 530.7 km<sup>2</sup> (Figure 1). Situated at the junction of two second-level geotectonic elements, i.e., the Kangdian axis (II<sub>1</sub>) and the Upper Yangtze Platform Fold Belt (II<sub>4</sub>), the study area has regional faults, and folds and faults characterize the structural trace. There are two main fault zones, i.e., the Zemuhe fault zone, through which the area from Hulukou to Qiaojia County passes, and the Xiaojiang fault zone, through which the area from Qiaojia County to Xiaojiang passes. Figure 2 shows the stratum development in the study area. We can see that the strata are well developed, including the Quaternary System (crushed stone mixed with soil, silt, and clay), Permian System (basalt, limestone, and sandstone), Carboniferous System (dolomite, limestone, and shale), Devonian System (limestone, dolomite, and sandstone), Silurian System (mudstone, sandstone, and shale), Ordovician System (dolomite and sandstone), Cambrian System (limestone, sandstone, and shale), Sinian System (dolomite, sandstone, and shale), and Presinian System (schist, phyllite, marble, slate, and limestone). The study area is in the lower reaches of the Jinsha River within the reservoir area, with a wide and gentle U-shape. The slopes on both banks are gentler on the bottom and steeper on the top. The bank slopes with elevations less than 900 m are relatively gentle, generally 10°–30°; the bank slopes with elevations greater than 900 m are steep, generally 30°–50°. There are many floodplains (both floodplains and river islands are widely distributed), terraces, and tablelands. In addition, the area is densely populated.

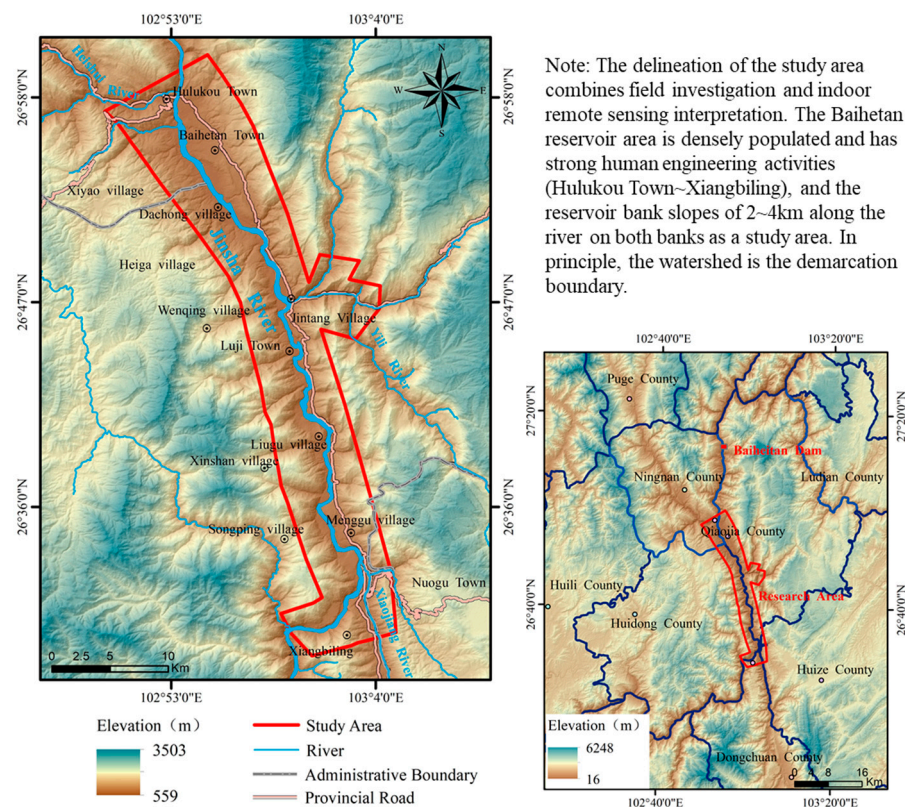
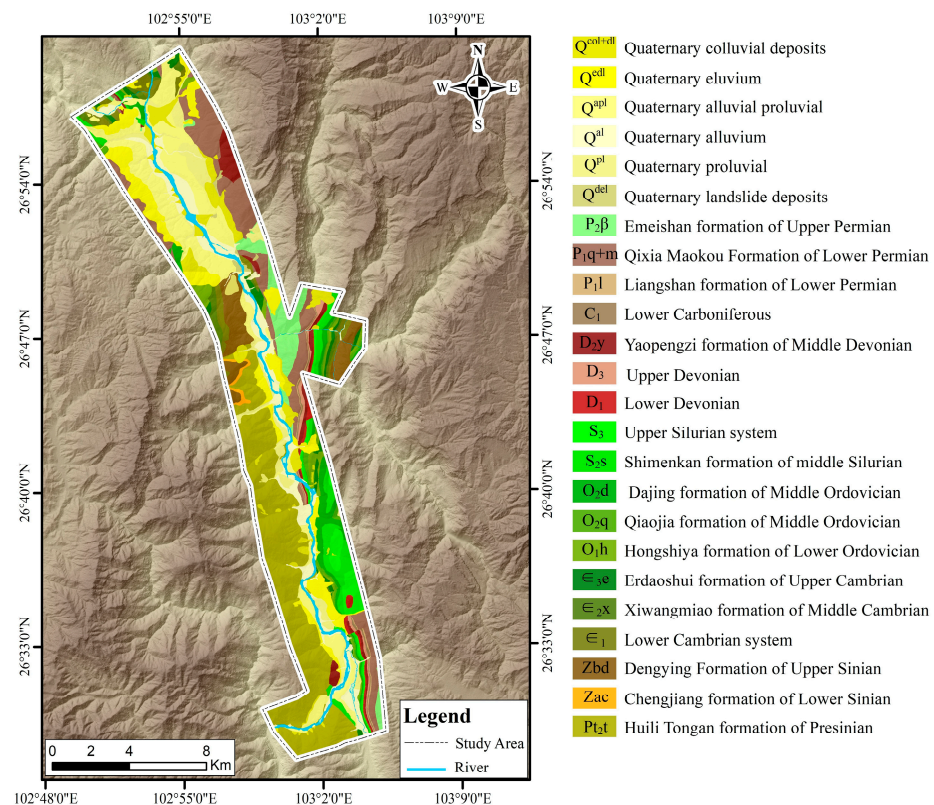


Figure 1. Geographical position map of the study area.



**Figure 2.** Regional geological map of the study area.

With a subtropical monsoon climate, the study area has a complex topography and large altitude differences. The climate is characterized by concentrated rainfall, distinctive seasons, a vertical climate gradient, and complex and variable microclimates. The annual average temperature ranges from 12 °C to 20 °C. It rains extensively between June and October, mostly in June, July, August, and September, accounting for more than 90% of the total precipitation of the year. Geological disasters in the study area have mostly occurred during this wet period.

### 3. Data and Methodology

#### 3.1. Data

The surface of the study area is covered with low and medium vegetation. To analyze the detection ability of satellites with different bands in the study area and avoid the omission and wrong judgment of landslide detection at different times [4], this study uses L-band ALOS PALSAR ascending orbit images (18 scenes) from 7 February 2007 to 18 November 2010, C-band Sentinel-1A ascending orbit images (86 scenes) from 19 October 2014 to 12 August 2020, and Sentinel-1A descending orbit images (56 scenes) from 19 February 2017 to 26 August 2020. SAR images are able to cover the entire study area (Figure 3). The basic parameters of the SAR data are shown in Table 1.

SAR data should be processed with reference to digital elevation model (DEM) data. As external data, DEM data can provide reference terrain or a geographic coordinate system to remove the influence of the topographic phase [24]. The DEM used in this study comes from the ALOS 12.5 m DEM provided by the Japan Aerospace Exploration Agency (JAXA). The DEM is collected by ALOS PALSAR and can reach 12.5 m in horizontal and vertical resolutions. In addition, before processing the Sentinel-1A data, it is necessary to download precise orbital data for the corresponding time points and import relevant data for correction of the orbit information to reduce the phase error caused by orbit error [25–27].

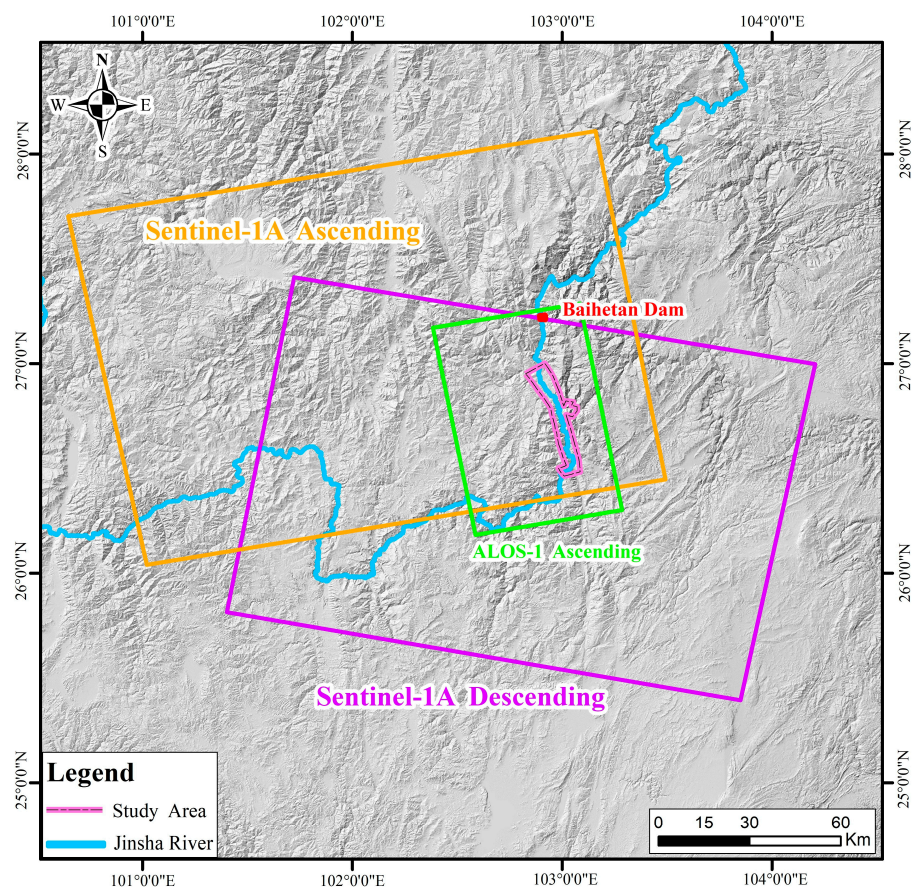


Figure 3. SAR data coverage in the study area.

Table 1. Basic parameters of SAR data in the study area.

Satellite	Wavelength	Ascending/ Descending Orbit	Time	Return to the Cycle	Resolution	Angle of Incidence	Imaging Mode	Polarization Mode
Sentinel-1A	5.6 cm/C Band	Ascending orbit	19 October 2014~ 12 August 2020	12 Days	20 m	43.9°	IW	VV
Sentinel-1A	5.6 cm/C Band	Descending orbit	19 February 2017~ 26 August 2020	12 Days	20 m	38.5°	IW	VV
ALOS PALSAR	23.6 cm/L Band	Ascending orbit	7 February 2007~ 18 November 2010	46 Days	20/10 m	39.6°	FBD /FBS	HH

### 3.2. Methodology

#### 3.2.1. Topographic Visibility

SAR is a side-looking imaging sensor. Since there is undulating terrain in the study area, the SAR data are subject to geometric restrictions that, to some degree, affect the order in which the radar echo signals reflected by the ground arrive at the imaging system. As a result, the SAR images from the imaging system are distorted, causing geometric distortion and thus seriously affecting the ability of SAR to monitor surface deformation. The geometric distortion is shown in Figure 4. When the satellite is in its ascending orbit, the slope faces west, southwest, or northwest ( $202.5^{\circ}$ – $337.5^{\circ}$ ), and the angle of slope is less than the local incidence angle of the satellite, the image length on the slope is shortened during SAR imaging. The distance  $cd$  in Figure 4 is less than the actual distance  $CD$ , causing foreshortening. When the slope faces southwest, west, or northwest ( $202.5^{\circ}$ – $337.5^{\circ}$ ) and the angle of slope is greater than the local incidence angle of the satellite, the top of the slope is imaged in the sensor before the bottom of the slope. Thus, the top point  $B$  of plane  $AB$  in Figure 4 is imaged earlier than point  $A$  on the ground, causing layover. When the

slope faces northeast, east, or southeast ( $22.5^{\circ}$ – $157.5^{\circ}$ ) and the angle of slope is greater than the complementary angle of the local incidence angle of the satellite, the satellite is unable to image this slope (plane GH in Figure 4), causing shadow. The direction of movement of the satellite causes the surface deformation along the south-north direction to have a very small projection along the direction of the LOS. This projection leads to the poor quality of the surface deformation along the south-north direction, resulting in low sensitivity. The other zones have high visibility. The visibility of the satellite in descending orbit is opposite that of the satellite in ascending orbit.

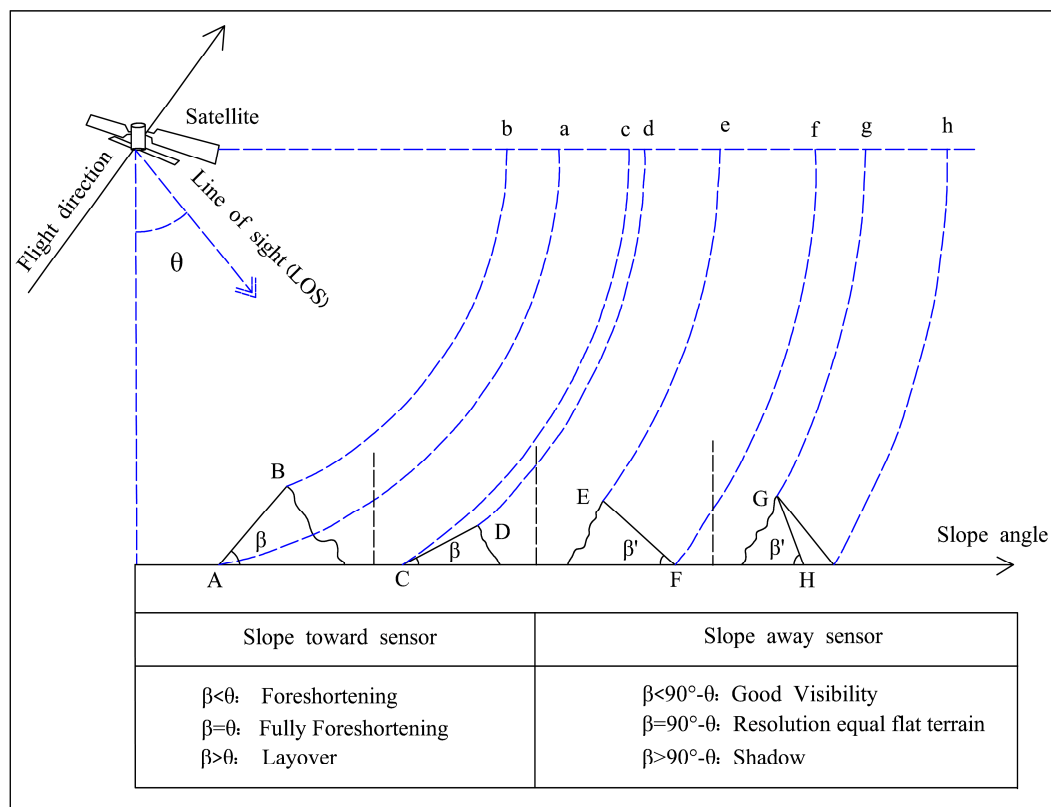


**Figure 4.** Geometric distortion diagram of radar side view imaging [28].

The visibility analysis of the study area depends on the topographic slope, aspect, and geometric parameters of the satellite (the incidence angle of the Sentinel-1A ascending orbit =  $43.9^{\circ}$ , the incidence angle of the Sentinel-1A descending orbit =  $38.5^{\circ}$ , and the incidence angle of the ALOS PALSAR ascending orbit =  $39.6^{\circ}$ ). The specific procedures are as follows: (1) reclassify the DEM of the study area into four types by slope gradient and aspect (aspect: due north ( $0^{\circ}$ – $22.5^{\circ}$ ,  $337.5^{\circ}$ – $360^{\circ}$ ), due south ( $157.5^{\circ}$ – $202.5^{\circ}$ ), due east, northeast, and southeast ( $22.5^{\circ}$ – $157.5^{\circ}$ ), or due west, southwest, and northwest ( $202.5^{\circ}$ – $337.5^{\circ}$ )); (2) use ArcGIS to extract three types of conditions, including whether the slope angle is greater than the satellite's local incidence angle, smaller than the satellite's local incidence angle, or greater than the complementary angle of the satellite's local incidence angle; and (3) use the Raster Calculator of ArcGIS to calculate and extract the relevant area of the geometric distortions.

### 3.2.2. InSAR Processing

To efficiently and appropriately process the large amount of SAR data obtained, the SBAS module in SARscape was used for semiautomated processing. The principle of the SBAS method is to use a high-coherence point to restore the time series of the deformation and to obtain interference pairs by connecting multiple pairs of parent and child images through short spatial-temporal baselines to generate small baseline sets

composed of multiple pairs of interference patterns based on the SAR data of each scene and the differential interference of the SAR data acquired at different times. Then, the singular-value decomposition (SVD) method is used to combine the data of multiple small baseline sets to find the solution [29] and to obtain the least-square solution of the minimum norm of the surface deformation rate between image sequences [30].

Before SAR image interference, the SAR image needs to be preprocessed through the following three steps. First, Sentinel-1A SAR data and the corresponding precise orbital data are imported simultaneously. Importing precise orbital data can reduce the phase error caused by an orbital error during InSAR processing and thus improve the accuracy of the data positioning. Since the original satellite data of ALOS PALSAR have radiation and geometric correction parameters, the reflectivity of each point in the original data must be focused by utilizing the optimized focusing algorithm, and then the output is the single look complex (SLC) data. Second, to reduce the data processing time, the original SAR image needs to be cut to a range larger than the study area. In this test, cutting, based on the geographic coordinate system, is performed on the original SAR image, with the DEM area larger than the study area and the vector files of the study area. Finally, before differential interference is conducted, the imported image data must be paired and connected to generate a connection diagram. Based on the Sentinel-1A satellite sensor type and personal experience, to prevent the pairing of images with an overly large time span, the Sentinel-1A ascending space baseline threshold should be set as 3% and that of the time baseline as 72 d (Figures 5 and 6). To pair the Sentinel-1A descending data, we set the threshold of the space baseline as 4% and that of the time baseline as 72 d (Figures 7 and 8). When the ALOS PALSAR satellite data are paired, since this satellite has L-band SAR with a long wavelength so that it can maintain coherency over a long period, the threshold of the time baseline should be 400 d, and that of the space baseline should be 50% of the threshold of the critical baseline (Figures 9 and 10). To obtain an accurate interferometric phase, the images should be registered prior to differential interference. During this process, the corresponding pixels of the parent and child images are accurately matched by translating and rotating images of the same coverage area. Generally, the matching accuracy should be at least 1/8 pixels [31].

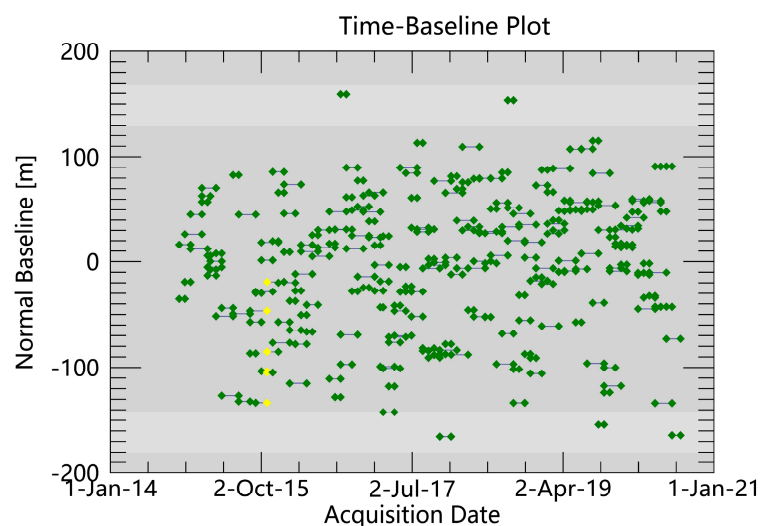


Figure 5. Time-Baseline map of Sentinel-1A ascending data.

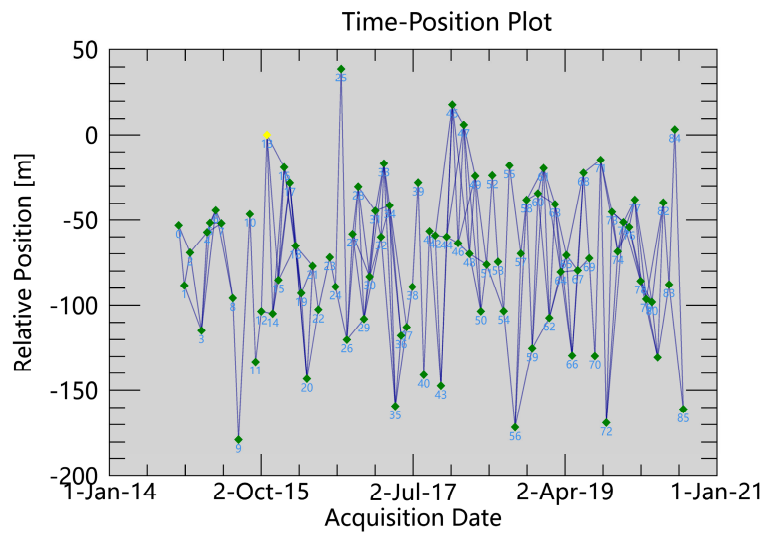


Figure 6. Time-Position map of Sentinel-1A ascending data.

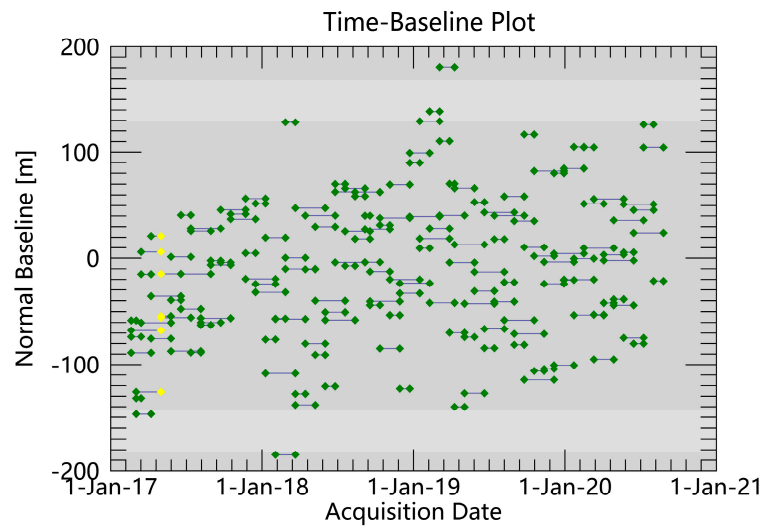


Figure 7. Time-Baseline map of Sentinel-1A descending data.

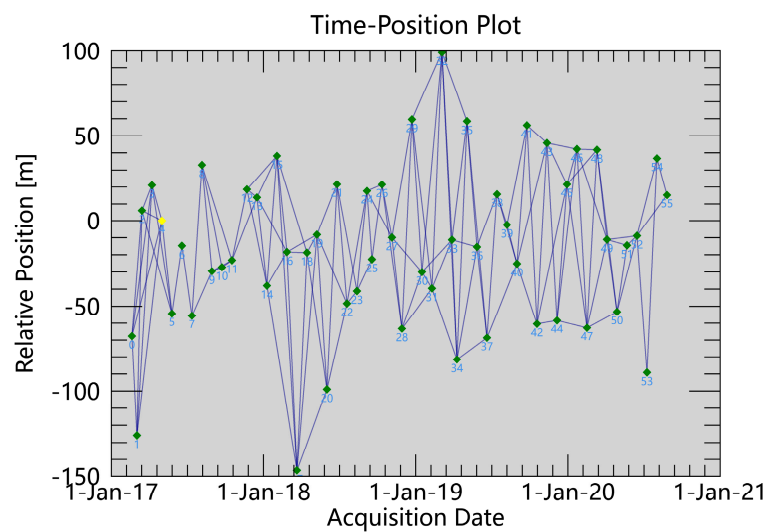


Figure 8. Time-Position map of Sentinel-1A descending data.

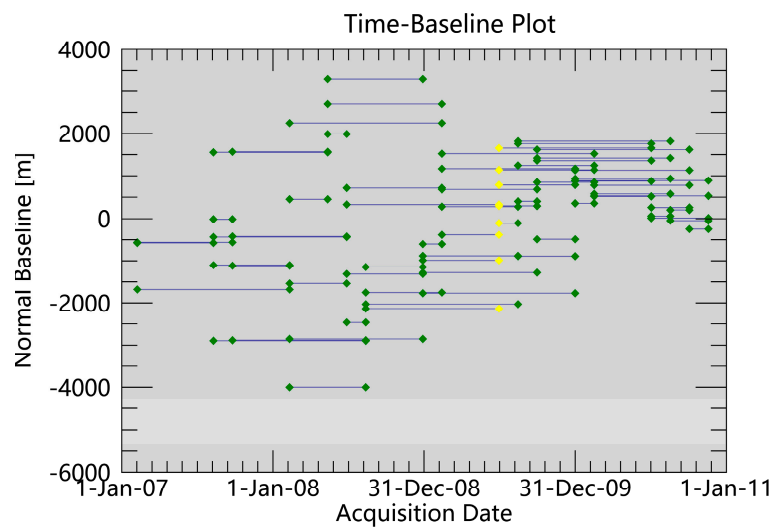


Figure 9. Time-Baseline map of ALOS PALSAR ascending data.

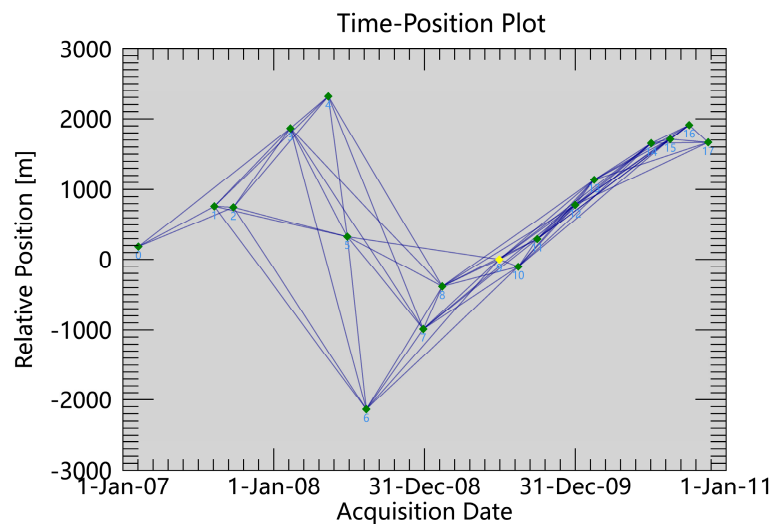


Figure 10. Time-Position map of ALOS PALSAR ascending data.

After the SAR image is preprocessed, interferometric communication, orbit reflat-tening, two inversions, and geocoding should be conducted to obtain the deformation. The specific processing steps are as follows. The interference communication in the ENVI SARscape software includes interferogram generation, flat-earth phase removal, filtering, and phase unwrapping. To remove noise during interference communication, a multilook ratio calculation is first performed. The ratio of the azimuth looks to range looks is set as 5:1 for Sentinel-1A and 1:3 for ALOS PALSAR. The Goldstein filtering algorithm, which can effectively inhibit phase noise, is applied to filter the SAR images. The study area is located in a mountainous area with poor coherence and even dense vegetation. Thus, to remove as much of the noise as possible, when the filtering parameters were set, the ratio of the minimum filtering value to the maximum filtering value was increased, the maximum and minimum sentinel data filtering thresholds were set as 5 and 8, respectively, and the maximum and minimum ALOS PALSAR data filtering thresholds were set as 6 and 9, respectively. Finally, the minimum cost flow algorithm was applied in phase unwrapping. To estimate and remove the constant phase and phase jump remaining in the unwrapped phase diagram, orbit reflat-tening of the results was conducted after interference communication, the linear optimization method was used for calculation, and the estimated phase ramp was directly removed from the unwrapped phase diagram.

Then, two inversions were performed. The first inversion was conducted to obtain the residual landform and deformation rate (estimated by the SVD method). The second inversion, based on estimating the deformation rate during the first inversion, removed the atmospheric phase by filtering. The atmospheric delay phase showed high-frequency signals in the time domain and low-frequency signals in the space domain [32–34]. With the removal of the atmospheric delay phase, the amount of deformation in the time series was eventually obtained. Finally, geocoding was performed. The deformation under the SAR coordinates obtained through the previous step was transformed into deformation under the geographic coordinates. The overall flow of the InSAR data processing is shown in Figure 11.

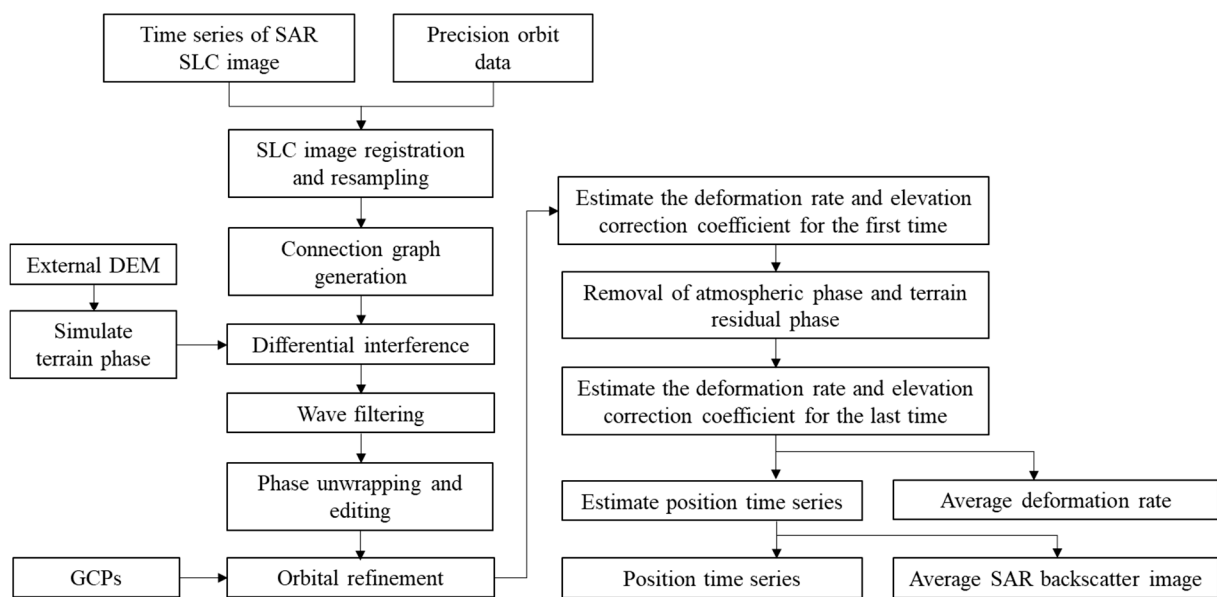


Figure 11. Flowchart of SBAS method.

## 4. Results and Analysis

### 4.1. Topographic Visibility Results

The visibility distribution of the SAR satellites in the study area was obtained based on the slope gradient, aspect, and incidence angle of the satellite along the direction of the LOS (Figures 12–14).

The area of geometric distortion (shadows, layover, and foreshortening) within the study area of the Sentinel-1A satellite in ascending orbit was 216 km<sup>2</sup>, accounting for 40.7% of the study area; the area of the low-sensitivity region was 122.5 km<sup>2</sup>, accounting for 23.1% of the study area. For the Sentinel-1A satellite in descending orbit, the area of geometric distortion (shadows, layover, and foreshortening) within the study area was 226 km<sup>2</sup>, accounting for 42.6% of the study area; the area of the low-sensitivity region was 122.5 km<sup>2</sup>, accounting for 23.1% of the study area. For the ALOS PALSAR satellite in ascending orbit, the area of geometric distortion (shadows, layover, and foreshortening) within the study area was 222.4 km<sup>2</sup>, accounting for 41.9% of the study area; the area of the low-sensitivity region was 122.5 km<sup>2</sup>, accounting for 23.1% of the study area. The InSAR technique was not effective in monitoring the above areas.

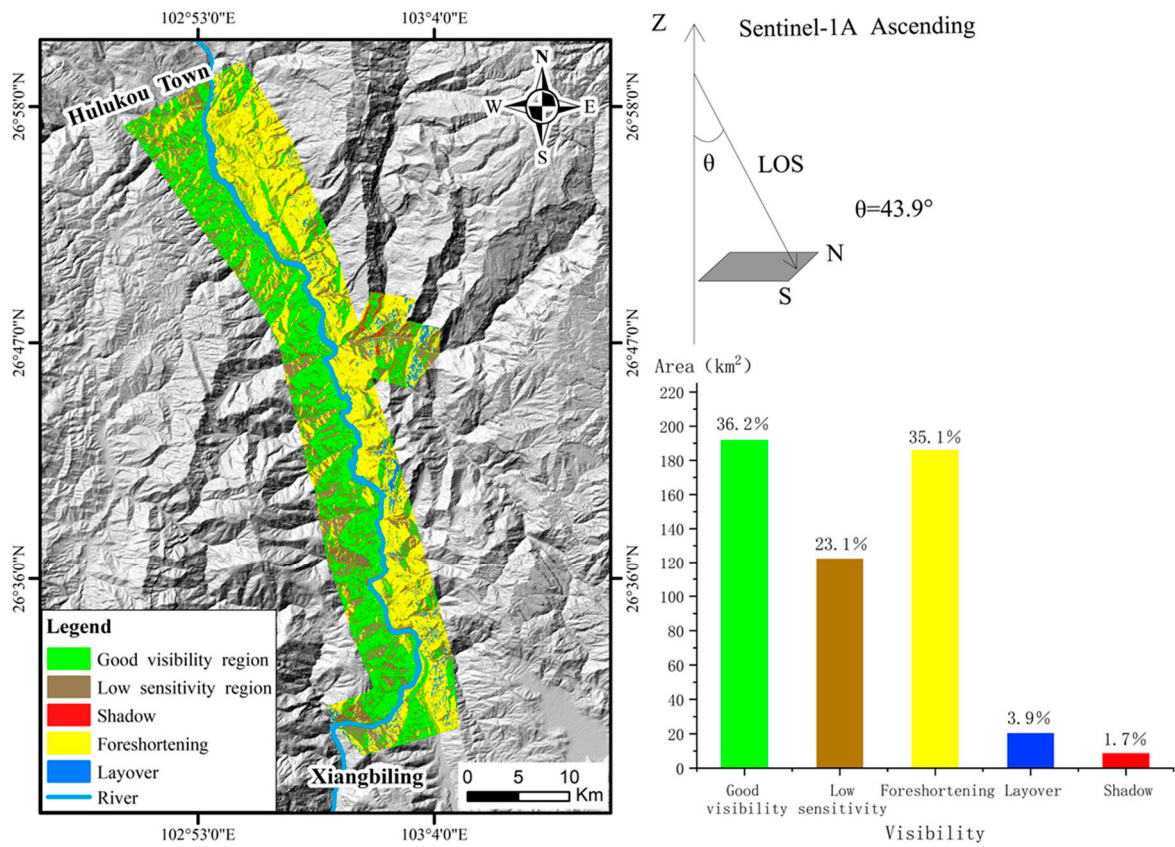


Figure 12. Visibility results of sentinel-1A ascending data in the study area.

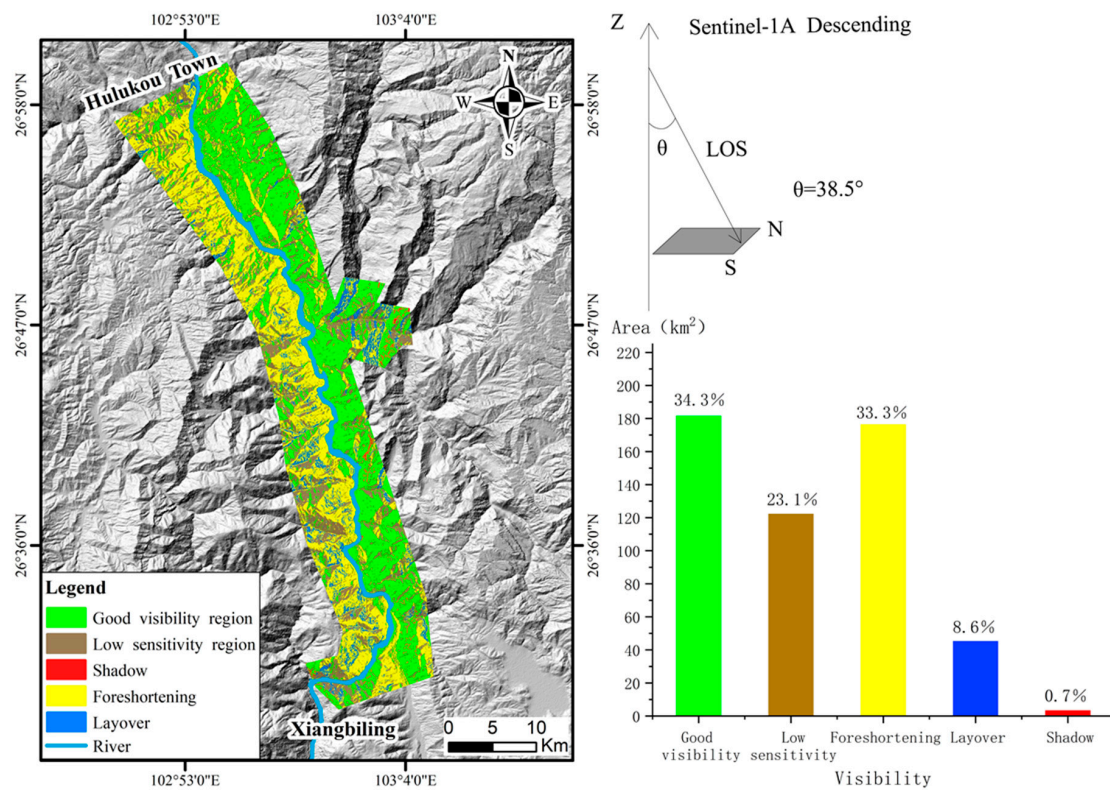


Figure 13. Visibility results of sentinel-1A descending data in the study area.

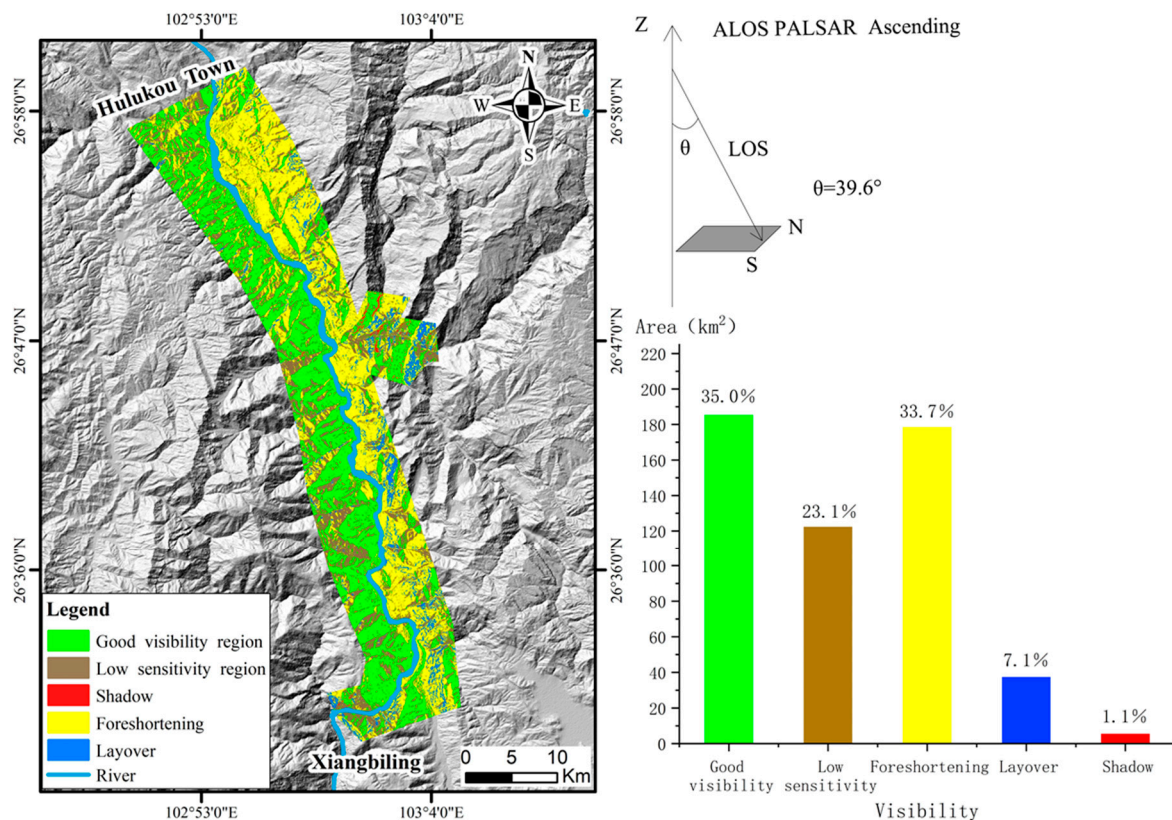


Figure 14. Visibility results of ALOS PALSAR ascending data in the study area.

According to Table 2 (comparison of SAR data observation information), it is difficult for a single-orbit satellite to obtain information about deformation in almost all directions in the study area. The effective observation area comprised 36.8% of the Sentinel-1A ascending data, 34.3% of the Sentinel-1A descending data, and 35% of the ALOS PALSAR ascending data. In contrast, monitoring by the Sentinel-1A satellite in both ascending and descending orbits improved the effective deformed area to 71.1%, which increased the detection rate of effective deformation information in the study area. As shown in Figures 12–14, for the satellite in ascending orbit, both the layover and foreshortened areas were mainly on the westward slopes, while the shadowed areas mainly occurred on the eastward slopes. For the satellite in descending orbit, both the layover and foreshortened areas were mainly on the eastward slopes, while the shadowed areas mainly occurred on the westward slopes. Therefore, both ascending and descending orbits should be used for InSAR deformation monitoring in the study area to reduce the effect of geometric distortion on the deformation results as much as possible. It can help us obtain abundant effective deformation information along the direction of the LOS within the study area.

Table 2. SAR data observation information ratio.

Observation	ALOS PALSAR Ascending	Sentinel-1A Ascending	Sentinel-1A Descending
Shadow	1.1%	1.7%	0.7%
Layover	7.1%	3.9%	8.6%
Foreshortening	33.7%	35.1%	33.3%
Geometric distortion region	41.9%	40.1%	42.6%
Low sensitivity region	23.1%	23.1%	23.1%
Effective deformation region	35%	36.8%	34.3%
Effective deformation region(fusion ascending and descending data)			71.1%

#### 4.2. Deformation Detection Results

When the area of geometric distortion generated by different SAR data in the study area was masked, ineffective points of deformation did not appear in the final processing results. Ultimately, the deformation results of the effective area along the direction of the LOS were obtained (Figures 15–17). In particular, the Sentinel-1A satellite in ascending orbit identified 15 deformed areas, i.e., H1-H15 in Figure 15; the Sentinel-1A satellite in descending orbit identified 11 deformed areas, i.e., H02, H04, H06, H12-H14, H16, and H17-H20 in Figure 16. Comparing these two results, we find that six deformed areas (H02, H04, H06, and H12-H14) resulted from the joint interpretation of the two orbits. The ALOS PALSAR ascending satellite identified 15 deformed areas, i.e., H03-H09, H11-H13, and H21-H25 in Figure 17; 5 more deformed areas (H21-H25) were identified than in the interpretation results of the ascending and descending orbits of Sentinel-1A. It shows that H21~H25 deformation area was in a state of slow deformation during the ALOS PALSAR monitoring period (7 February 2007 to 18 November 2010). However, during the Sentinel-1A monitoring period, the H21~H25 area may have been in a stable state without slow deformation. The effect of the reservoir water during and after impoundment is likely to induce the deformation of the H21~H25 area again, thus affecting the stability of the slopes and threatening the safe operation of the reservoir area. (A negative value implies that the surface feature moves away from the satellite along with the radar LOS; a positive value indicates that the surface feature moves toward the satellite along with the radar LOS.)

The ALOS PALSAR ascending orbit detected that most bank slopes in the study area were significantly deformed between 2007 and 2010, but the deformation results were less significant than those between 2014 and 2020. The deformation results detected by the Sentinel-1A ascending orbit indicate that the construction of the main station of the hydropower project after 2013 caused obvious disturbances to the stability of the bank slopes in the study area. Most deformation rates in the study area were within the range of  $-10$ – $10$  mm/a between 2014 and 2020. The slopes within this range of deformation rates were generally stable. The maximum deformation rate reached 78 mm/a.

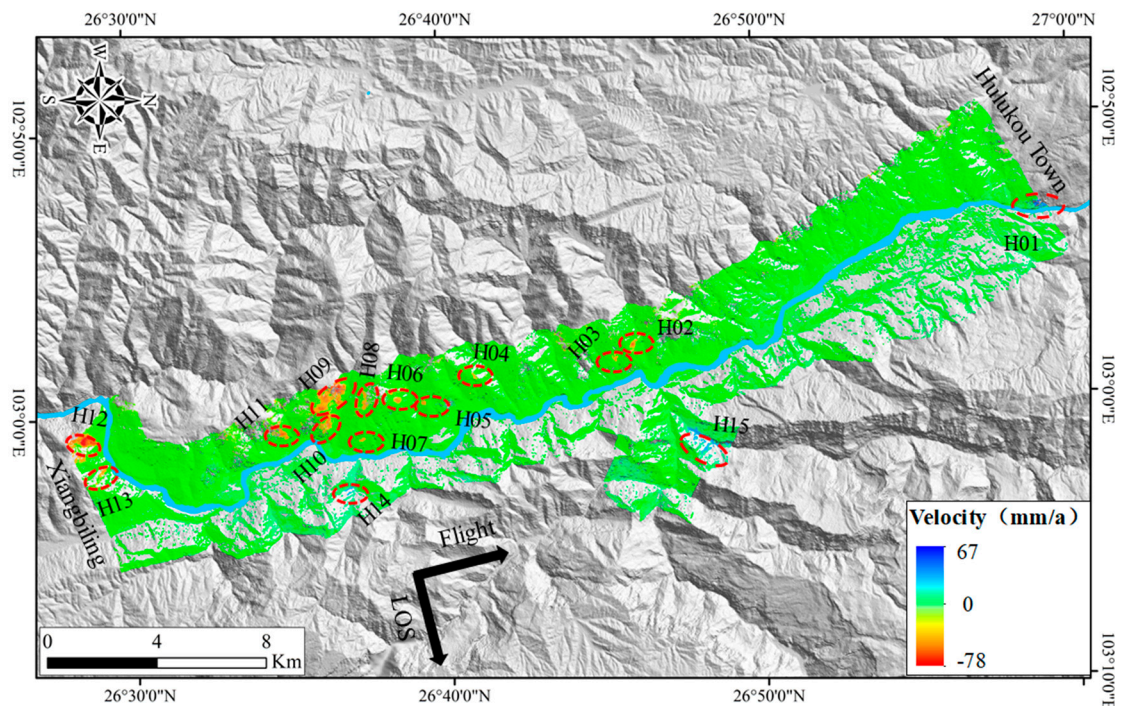


**Figure 15.** Effective deformation results of Sentinel-1A ascending data in the study area.

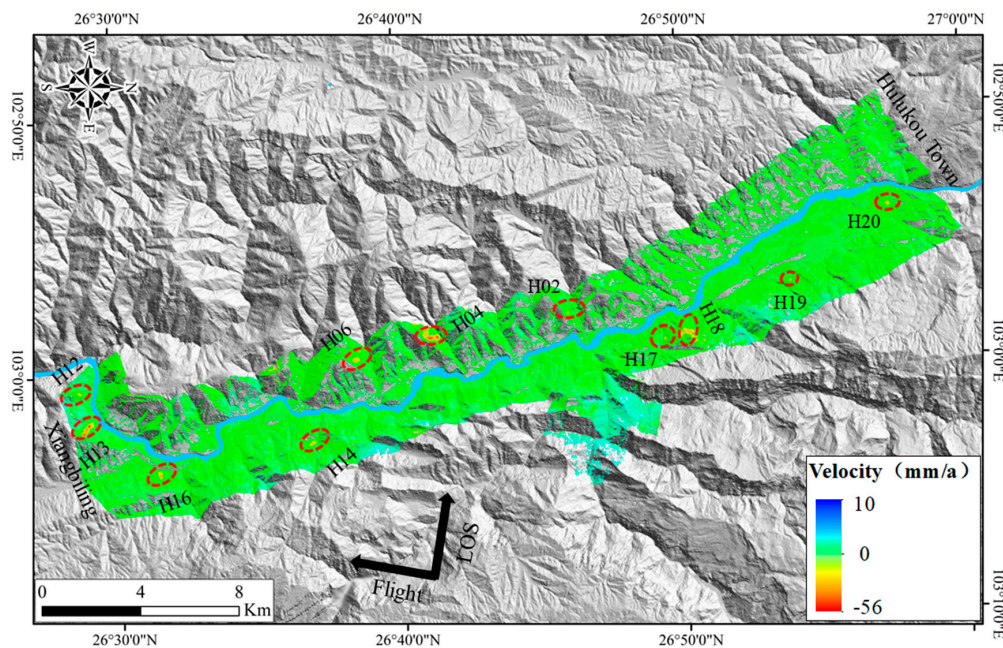


**Figure 16.** Effective deformation results of Sentinel-1A descending data in the study area.

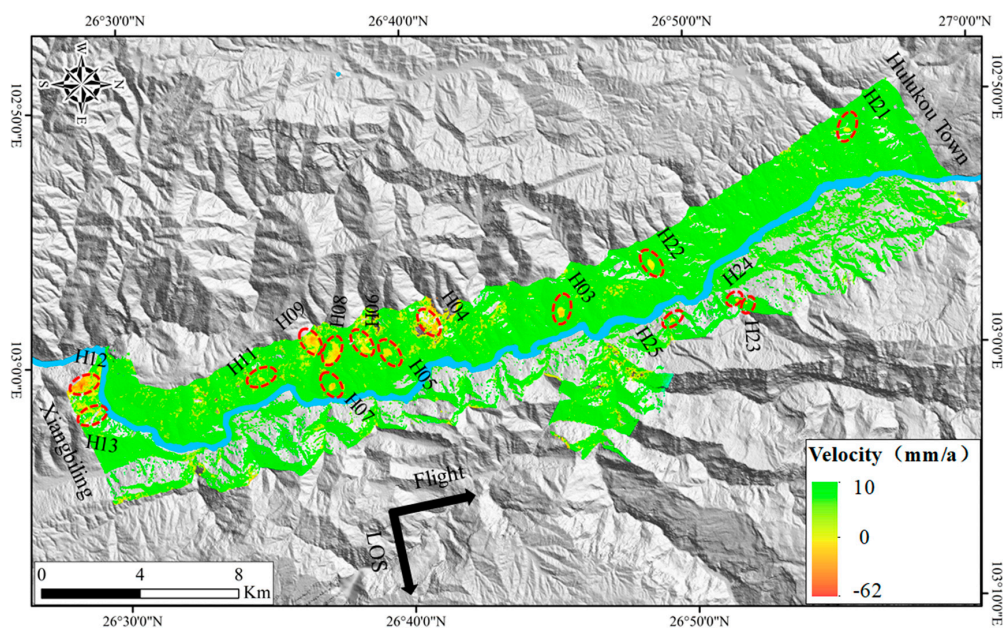


**Figure 17.** Effective deformation results of ALOS PALSAR ascending data in the study area.

#### 4.3. Mapping Active Landslides

Because InSAR deformation results can only detect the active area and cannot accurately determine whether it is a landslide and the boundary range of a landslide, landslides should be identified with the InSAR results in combination with optical remote sensing images, and the identification results need to be verified by field investigation. The landslide indicators of optical image recognition can be classified as morphological and microtopography features. The morphological features were as follows: (1) The back walls of the landslides were mostly round-backed, armchair-shaped, and curved; (2) the slope surfaces were mostly straight, concave, convex, and stepped; and (3) the slope bodies were mostly semicircular, rectangular, tongue-shaped, and elliptical. The microtopography features were as follows: (1) The fissures at the front edge and in the middle of the landslides

exhibited abnormal color tones and textures; (2) the rock and soil mass in the middle and at the front edge of the landslide were prone to fissures and mostly exhibited dark tones in images; and (3) the slopes on both sides of the valley were high and steep [35]. The deformed areas identified by the timing SBAS-InSAR technique were combined with the landslide indicators of optical image recognition to delineate the landslide boundaries in Google Earth images, and a total of 25 active landslides were recognized.

Field review and verification of the results of indoor interpretation were performed using field reconnaissance, unmanned aerial vehicle-assisted surveys, etc. Due to the low resolutions and slow image updates of Google Earth images and other factors, the landslide disaster boundary range of indoor interpretation was slightly different from the field survey results. Seven of the 25 deformed areas identified in common by the Sentinel-1A ascending and descending orbits and the ALOS PALSAR ascending orbit were caused by human engineering activities, among which the construction of highways was the main cause of deformation due to human engineering activities. Two of the remaining 18 deformed areas were landslide disaster clusters (H04 and H15). Ultimately, 21 active landslide disaster points were identified, of which 14 active landslides were newly added, i.e., H01, H03, H04-1~H04-2, H08~H09, H13~H14, H15-1~H15-3, H17, and H21~H22. The deformation characteristics of different active landslide disaster points vary, with rock mass fragmentation, crack development and multistage dislocation as the main deformation characteristics. Figure 18 shows part of the typical results of the landslide disaster identification and the outcome of the field verification. Information about deformation behavior is shown in Table 3. Table 4 presents the information on deformations caused by human engineering activities.

**Table 3.** Summary of information regarding active landslides.

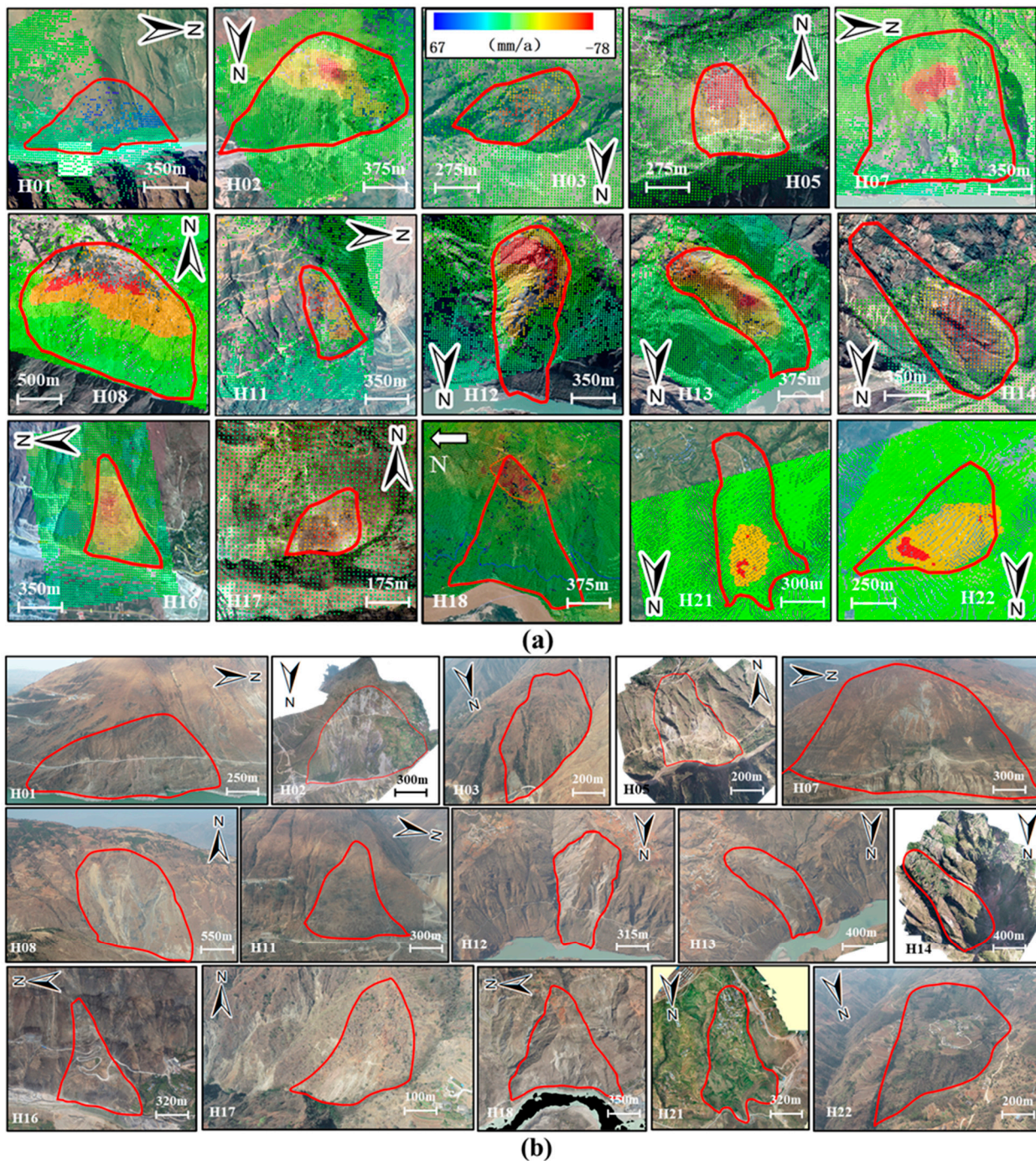
InSAR Deformation Area Number	Long (m)	Wide (m)	Slope (°)	Aspect (°)	Maximum Deformation Rate (mm/a)	Deformation Characteristics	
H01	500	960	23~30	80	67	The rock mass is broken, and the rock collapses in the deformation area	
H02	1180	1640	25~45	5	−56	There are many fractures and lower staggered scarps, with local collapses in the deformation area	
H03	780	500	22~34	48	−46	There are many lower staggered scarps and a three-step stepped topography in the deformation area	
H04	H04-1	650	380	16~39	320	−56	The rock mass is broken, and substantial bedrock collapse downward in the deformation area
	H04-2	660	440	28~46	340	−78	The rock mass is broken, and the road is cracked in the deformation area
H05	670	500	34~54	162	−39	The rock mass is broken, and the broken stone has collapsed in the deformation area	
H07	1340	1390	30~40	88	−49	The branch gullies are developed, the surface of the slope is seriously eroded, and the broken stone has collapsed downward in the deformation area	
H08	1530	1080	28~46	173	−45	The slope surface is weathered and eroded, and the rock and soil mass of the slope has collapsed in the deformation area	
H09	1330	600	40~56	38	−74	There is an obvious lower staggered scarp in the deformation area	
H11	520	360	28~40	73	−57	The bedrock is exposed, and the rock mass on the surface of the slope is relatively broken, with the local collapse in the deformation area	
H12	1680	430	40~58	320	−56	The rock mass is broken and loose, and the broken stone has collapsed downward in the deformation area	
H13	1740	620	40~60	22	−78	The fractures are well developed, and rock blocks have fallen in the deformation area	

Table 3. Cont.

InSAR Deformation Area Number	Long (m)	Wide (m)	Slope (°)	Aspect (°)	Maximum Deformation Rate (mm/a)	Deformation Characteristics
H14	1220	460	16~40	318	−37	There is a secondary sliding, and serious cracks appear in houses in the deformation area
H15	H15-1	700	30~40	282	30	There are many lower staggered scarps and small-scale landslides in the deformation area
	H15-2	660	40~50	323	32	The shallow surface of the slope has collapsed in the deformation area
	H15-3	600	40~55	280	35	The rock mass is broken, and the broken surface stone of the slope has collapsed downward in the deformation area
H16	930	660	15~50	258	−43	The retaining wall and the highway are cracked, and signs of deformation are obvious in the deformation area
H17	380	300	28~46	208	−33	There are lower staggered scarps and local collapses in the deformation area
H18	1300	1330	16~54	270	−36	Several fractures have developed in the deformation area
H21	1280	570	10~34	348	−32	Secondary sliding has occurred, and there was obvious dislocation in the deformation area
H22	780	840	16~40	27	−37	The building has cracked, and the platform was staggered in the deformation area

Table 4. Summary of information regarding human engineering activities.

InSAR Deformation Area Number	Maximum Deformation Rate (mm/a)	Causes of Deformation
H06	−47	The original stress of the rock and soil has changed, and the local collapse was caused by highway construction
H10	−50	The original stress of the rock and soil has changed, and the local collapse was caused by highway construction
H19	−28	Road construction, artificial excavation
H20	−36	The settlement deformation was caused by artificial excavation and heaped load
H23	−32	The original stress of the rock and soil has changed, and local collapse was caused by highway construction
H24	−29	The original stress of the rock and soil has changed, and local collapse was caused by highway construction
H25	−27	The construction of the tunnel has changed the original stress of the rock and soil mass and caused local collapse



**Figure 18.** (a) Deformation rate and remote sensing interpretation boundary of 15 typical active landslides (b) Fifteen typical active landslides were reviewed and photographed; The red line in the figure represents the landslide boundary. The base map in figure (a) is from Google Earth image.

## 5. Discussion

### 5.1. Distribution Pattern of the Detected Landslides

A variety of factors may affect disaster development, including intrinsic factors and extrinsic factors. However, since the present study area is in the wide valley of the Baihetan reservoir area, where the selected range of the study extended 2–4 km along both banks of the river, extrinsic factors such as elevation and slope had little effect on the development of landslides. The present study analyzed only the development and distribution patterns of

active landslides based on two factors, i.e., the formation of lithology and fault distribution in the geological background.

According to the relationship between the distribution of active landslides and the faults (Figure 19), 12 of the 21 active landslides within the study area were crossed by faults, i.e., H01, H02, H04-1, H04-2, H05, H07, H12, H13, H14, H17, H18, and H22. There were no faults around the nine active landslides, i.e., H03, H08, H09, H11, H16, H15-1, H15-2, H15-3, and H21. The field investigation revealed that the rock masses of active landslides crossed by and near the faults were relatively broken. Because the strong tensile forces and tensions exceeded the bearing capacity of the rock mass during fault formation; the resulting rock mass ruptures resulted in poor structural properties in the strata where the faults are located. These slopes are prone to deformation and instability under the influence of external factors [36].

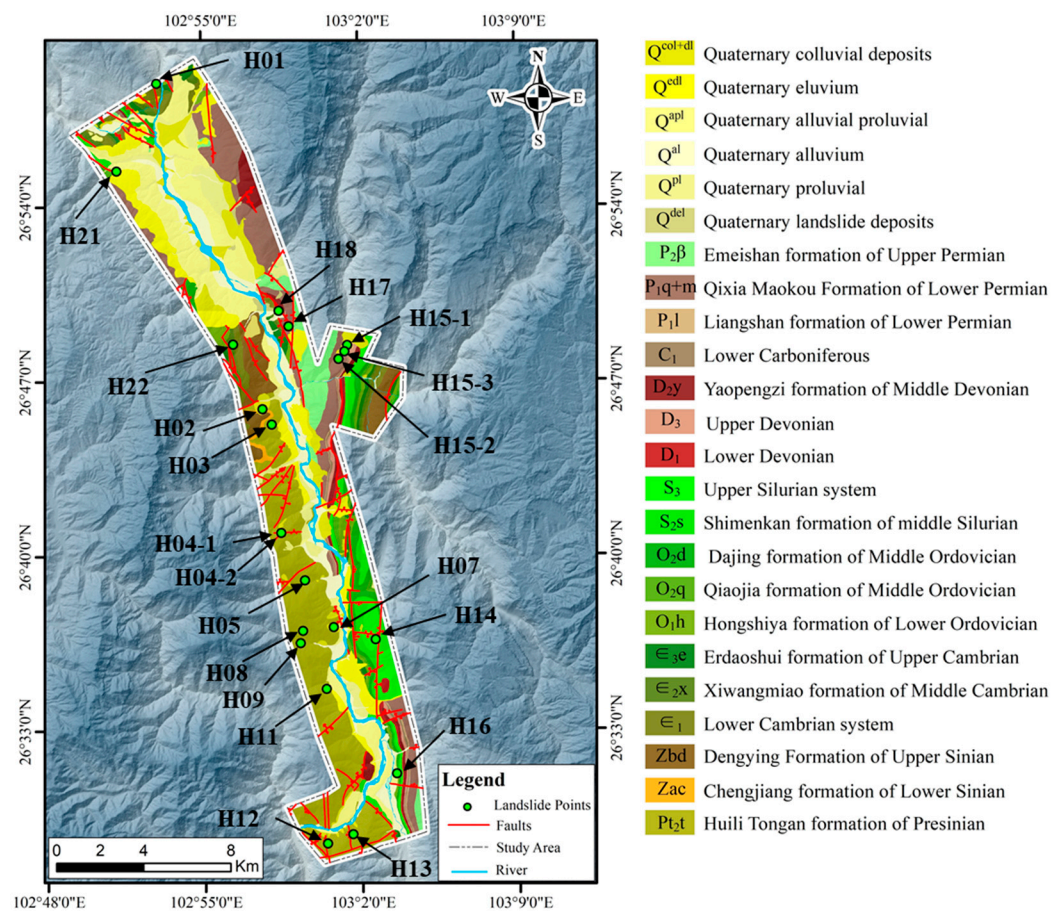


**Figure 19.** Development and distribution of active landslides.

The relationship between the distribution of the active landslides and strata indicates well-developed strata in the study area, from the Quaternary System of the Cenozoic through the Presinian System of the Lower Proterozoic, featuring complex formation lithology (Figure 19). Their hardnesses could classify the strata of the development into hard rock, relatively hard rock, relatively soft rock, soft rock, and extremely soft rock. Eight active landslides occurred in relatively soft to hard rock strata; six active landslides occurred in the relatively soft to relatively hard rock strata; two active landslides occurred in the soft to hard rock strata; and five active landslides occurred in the Quaternary strata. In conclusion, the strata where above active landslides developed were not purely hard and their strength of rock and soil masses were low. As a result, above landslides stability could frequently decrease under the action of external factors such as rainfall and earthquakes, leading to disasters.

According to the distribution pattern of active landslides analyzed with the above-described two factors, it can be concluded that most active landslides were controlled by faults, and rock masses of active landslides crossed by faults were relatively broken. The strata where active landslides developed were not controlled by faults are relatively weak. The joint actions of intrinsic and extrinsic conditions caused the identified landslides to be currently active at the time of the study.

### 5.2. Impact Factors of the Landslide Detection Results

We acquired three different kinds of SAR data and employed the SBAS-InSAR technique to identify the active landslides within the study area. This paper showed that the results of the InSAR-identified data varied depending on the different satellites and orbits. Since the Sentinel-1A ascending and descending orbit data and the ALOS PALSAR ascending data were acquired through side-looking imaging, the resulting LOS deformation information resulted in certain geometric distortion in the study area. The differences in slope gradients and aspects between the two banks and the differences in flight angles along the satellite orbits resulted in differences in the area distributions of the geometric distortion between the two banks. Regarding the satellites (ascending) that collected images in the same orbital direction with different radar sensors, with a constant increase in the LOS incidence angle of the radar satellite (Sentinel-1A > ALOS PALSAR), the layover area within the study area constantly decreased, the shadow and foreshortened areas constantly increased, and the total area of geometric distortion constantly decreased (Figure 20). To prevent a decrease in the area of the effective observation zone due to topographical effects, ascending and descending orbit data were combined to effectively reduce the areas that could not be effectively observed due to geometric distortion, thereby enhancing the effective detection rate of the satellite data. In addition, the combined use of ascending and descending orbit data in computation for some areas could facilitate auxiliary verification or three-dimensional deformation calculation.

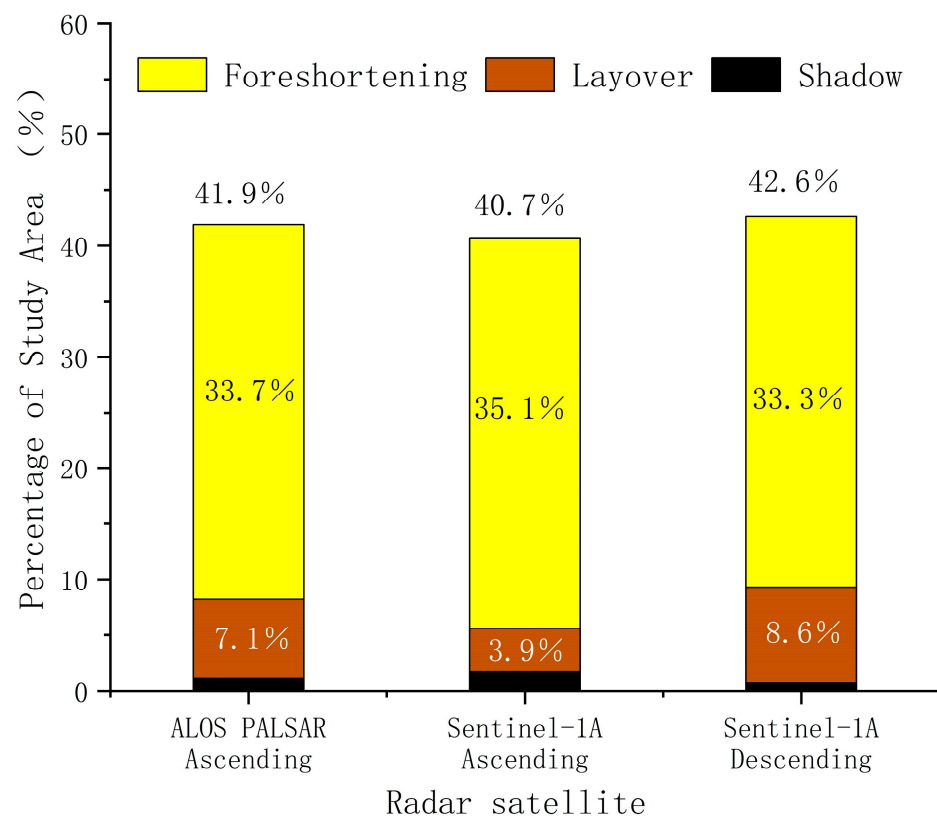


Figure 20. Percentage of different SAR data geometric distortion types in the study area.

According to recognition results from the Sentinel-1A ascending data and ALOS PALSAR ascending data (same type of orbit), more active landslide points were identified on the left bank, but there were still some differences in the identified results. The summary analysis offers the following causes:

- (1) Each kind of satellite data corresponds to different wavelengths. Sentinel-1A is a C-band radar satellite; the wavelengths of the C-band are shorter than the wavelengths of the ALOS PALSAR data. The Sentinel-1A data exhibit the poor ability to penetrate dense vegetation, which might affect the intensification of the echo signal and frequently result in decoherence effects; this may result in a zero deformation point in areas with dense vegetation, thereby distorting the differences in the monitoring results.
- (2) The two satellites acquired data at different times, so the deformation computed with InSAR reflects only the deformation results within the data acquisition period.
- (3) The vegetation penetration capabilities of the ALOS PALSAR data are higher than those of the Sentinel-1A data since the wavelengths of the ALOS PALSAR data are longer than those of the Sentinel-1A data. However, decoherence of the interference pattern also occurred because of the fewer ALOS PALSAR inventory data points for the study area, the excessively long acquisition time interval, and the poorer data continuity than Sentinel-1A. The amount of data and the acquisition interval of the data may have affected the final deformation results. The more SAR data involved in the InSAR calculation and the shorter and more continuous the intervals between each data acquisition, the better the deformation results are; for the opposite, the deformation results are poor.

In conclusion, the results of joint monitoring with Sentinel-1A ascending and descending orbits before impoundment in the study area were superior to the ALOS PALSAR ascending data monitoring results. ALOS PALSAR was significantly inferior to Sentinel-1A in both data continuity and data volume. For active landslide recognition and deformation monitoring of the study area during and after impoundment, where financial conditions permit, ALOS-2 data with relatively continuous observations and other radar satellite data with large LOS incidence angles could be purchased for some densely vegetated areas to enhance the accuracy of the overall recognition and monitoring results.

## 6. Conclusions

The intensely tectonized and well-developed strata of the densely populated bank segment between Hulukou and Xiangbiling within the Baihetan reservoir area will affect the stability of the bank slopes of the reservoir after impoundment. Therefore, it is extremely important to identify and analyze the active landslides in the study area before impoundment. Because of the complicated terrain in the study area, InSAR was used to acquire the LOS deformation results. Geometric distortion affected the deformation results, thereby resulting in incorrect judgments regarding the identification and analysis of landslides. Hence, the research area was subjected to visibility analysis based on the relationship between its related parameters and topographic factors by considering the image datasets of Sentinel-1A ascending and descending orbits and the different wavebands and orbits of ALOS PALSAR to quantify the areas of various geometric distortions and zones with high visibility. Since it is extremely difficult for single-orbit satellites to acquire deformation information, the combination of ascending and descending orbits can effectively reduce the areas that cannot be observed due to geometric distortion, thereby improving the satellite monitoring efficiency. It is advisable to choose SAR data with large LOS incidence angles during and after impoundment to minimize geometric distortions.

The untrusted areas resulting from geometric distortion were masked based on the terrain visibility of the SAR data to ultimately acquire real and effective deformation information based on the SBAS-InSAR technique. A total of 25 active landslides were identified based on the obtained deformation information and Google Earth remote sensing images, and an efficient and feasible method was established for the early identification

of active landslides. Field investigation and verification revealed 21 active landslides (including 14 new active landslides) and seven deformations caused by human engineering activities. Most of the identified active landslides were controlled by faults, and the rock mass of active landslides crossed by the faults was relatively broken. The strata where active landslides developed were not controlled by faults exhibited low strength. The joint actions of intrinsic effects and extrinsic conditions caused the identified landslide disasters to be currently active. For some areas with dense vegetation within the study area, it is advisable to purchase ALOS-2 data with relatively continuous observations for monitoring during and after impoundment to prevent excessive decoherence effects.

Our research provides technical support for the safe operation and disaster prevention and mitigation of the Baihetan Reservoir area during and after impoundment, which will provide relevant references for the future identification and analysis of regional active landslides under complex terrain in China and throughout the world. Our research will be beneficial to the development of landslide early warning systems in the mountainous southwestern areas of China.

**Author Contributions:** J.D. and X.Y. conceived the manuscript; J.D. dealt with InSAR data and drafted the manuscript; W.F. provided funding support and ideas; G.Z. conducted a field investigation and provided field data. M.W. provided field data. All authors have read and agreed to the published version of the manuscript.

**Funding:** This research was funded by the National Natural Science Foundation of China (Grant Nos. 41977252, U2005205), the State Key Laboratory of Geohazard Prevention and Geoenvironment Protection Independent Research Project (Grant No. SKLGP2020Z001), and the Zhejiang Huadong Construction Engineering Co., Ltd Research Project (KY2020-HDJS-19).

**Acknowledgments:** We are very grateful to sentinel-1A data provided by European Space Agency (ESA), ALOS PALSAR data provided by Japan Aerospace Research and Development Agency (JAXA), and 12.5m resolution "ALOS World 3D-12.5m" DEM provided by Japan JAXA. We also thank Zhejiang East China Construction Engineering Co., Ltd. and relevant comrades for their help.

**Conflicts of Interest:** The authors declare no conflict of interest.

## References

1. Qiao, P. Research on Revival Mechanism and Stability of Meilishi 3# Giant Landslide of Gushui Hydropower Station on Lancang River. Master's Thesis, Chengdu University of Technology, Chengdu, China, 12 July 2016.
2. Wang, S.; Xu, W.; Liu, J. Stability and failure mechanism analyses of the Zhenggang landslide in southwestern China. *Adv. Civ. Eng.* **2018**, *2018*, 1–16. [[CrossRef](#)]
3. Zhou, J.; Shi, C.; Xu, F.G. Geotechnical characteristics and stability analysis of rock-soil aggregate slope at the Gushui Hydropower Station. *Southwest China Sci. World J.* **2013**, *2013*, 540636. [[CrossRef](#)]
4. Kang, Y.; Zhao, C.; Zhang, Q.; Lu, Z.; Li, B. Application of InSAR techniques to an analysis of the Guanling landslide. *Remote Sens.* **2017**, *9*, 1046. [[CrossRef](#)]
5. Yi, X.Y.; Feng, W.K.; Bai, H.L. Catastrophic landslide triggered by persistent rainfall in Sichuan, China: August 21, 2020, Zhonghaicun landslide. *Landslides* **2021**, *18*, 2907–2921. [[CrossRef](#)]
6. Burgmann, R.; Rosen, P.A.; Fielding, E.J. Synthetic aperture radar interferometry to measure Earth's surface topography and its deformation. *Annu. Rev. Earth Planet Sci.* **2000**, *28*, 169–209. [[CrossRef](#)]
7. Dong, J.; Liao, M.; Xu, Q.; Zhang, L.; Tang, M.; Gong, J. Detection and displacement characterization of landslides using multi-temporal satellite SAR interferometry: A case study of Danba County in the Dadu River. *Eng. Geol.* **2018**, *240*, 95–109. [[CrossRef](#)]
8. Shi, X.G.; Yang, C.; Zhang, L.; Jiang, H.J.; Liao, M.S.; Zhang, L.; Liu, X.G. Mapping and characterizing displacements of active loess slopes along the upstream Yellow River with multi-temporal InSAR datasets. *Sci. Total Environ.* **2019**, *674*, 200–210. [[CrossRef](#)] [[PubMed](#)]
9. Shi, X.G.; Liao, M.S.; Li, M.H.; Zhang, L.; Cunningham, C. Wide-area landslide deformation mapping with multi-path ALOS PALSAR data stacks: A case study of three gorges area, China. *Remote Sens.* **2016**, *8*, 136. [[CrossRef](#)]
10. Zhao, C.Y.; Liu, X.J.; Zhang, Q.; Peng, J.B.; Xu, Q. Research on loess landslide identification, monitoring and failure mode with InSAR technique in Heifangtai, Gansu. *Geomat. Inf. Sci. Wuhan Univ.* **2019**, *44*, 996–1007. (In Chinese) [[CrossRef](#)]
11. Dai, C.; Li, W.L.; Lu, H.Y.; Yang, F.; Xu, Q.; Jian, J. Landslides detection using InSAR technology, A Case Study in Zhouqu County, Gansu Province, China. *Geomat. Inf. Sci. Wuhan Univ.* **2020**, *44*, 996–1007. (In Chinese) [[CrossRef](#)]
12. Shi, X.G.; Zhang, L.; Tang, M.G.; Li, M.H.; Liao, M.S. Investigating a reservoir bank slope displacement history with multi-frequency satellite SAR data. *Landslides* **2017**, *14*, 1961–1973. [[CrossRef](#)]

13. Li, M.; Zhang, L.; Shi, X.; Liao, M.; Yang, M. Monitoring active motion of the Guobu landslide near the Laxiwa Hydropower Station in China by time-series point-like targets offset tracking. *Remote Sens. Environ.* **2019**, *221*, 80–93. [[CrossRef](#)]
14. Zhang, Y.; Meng, X.; Jordan, C.; Novellino, A.; Dijkstra, T.; Chen, G. Investigating slow-moving landslides in the Zhouqu region of China using InSAR time series. *Landslides* **2018**, *15*, 1299–1315. [[CrossRef](#)]
15. Meisina, C.; Zucca, F.; Notti, D. Geological interpretation of PSInSAR data at regional scale. *Sensors* **2008**, *8*, 7469–7492. [[CrossRef](#)]
16. Xu, W.Y.; Zhang, Q.; Zhang, J.C.; Wang, R.B.; Wang, R.K. Deformation and control engineering related to huge landslide on left bank of Xiluodu reservoir, south-West China. *Eur. J. Environ. Civ. Eng.* **2013**, *17*, 249–268. [[CrossRef](#)]
17. Zhao, C.Y.; Lu, Z.; Zhang, Q.; de la Fuente, J. Large-area landslide detection and monitoring with ALOS/PALSAR imagery data over northern California and southern Oregon, USA. *Remote Sens. Environ.* **2012**, *124*, 348–359. [[CrossRef](#)]
18. Zhang, Y.; Meng, X.M.; Dijkstra, T.A.; Jordan, C.J.; Chen, G.; Zeng, R.Q.; Novellino, A. Forecasting the magnitude of potential landslides based on InSAR techniques. *Remote Sens. Environ.* **2020**, *241*, 111738. [[CrossRef](#)]
19. Bianchini, S.; Cigna, F.; Righini, G. Landslide HotSpot Mapping by means of Persistent Scatterer Interferometry. *Environ. Earth Sci.* **2012**, *67*, 1155–1172. [[CrossRef](#)]
20. Zhao, C.Y.; Kang, Y.; Qin, Z.; Zhong, L.; Bin, L. Landslide Identification and Monitoring along the Jinsha River Catchment (Wudongde Reservoir Area), China, Using the InSAR Method. *Remote Sens.* **2018**, *10*, 993. [[CrossRef](#)]
21. Lu, H.Y.; Li, W.L.; Xu, Q.; Dong, X.J.; Dai, C.; Wang, D. Early detection of landslides in the upstream and downstream areas of the Baige Landslide, the Jinsha River based on optical remote sensing and InSAR technologies. *Geomat. Inf. Sci. Wuhan Univ.* **2019**, *44*, 1342–1354. (In Chinese) [[CrossRef](#)]
22. Zhang, Y. Detecting Ground Deformation and Investigating Landslides Using InSAR Technique—Taking Middle Reach of Bailong River Basin as an Example. Ph.D. Thesis, Lanzhou University, Lanzhou, China, 2018.
23. Chen, L. Study on the Influence of Reservoir Water Storage on the Stability of Reservoir Bank—Take Baihetan Area of Ningnan County as an Example. Master’s Thesis, Chang’an University, Xi’an, China, 21 July 2016.
24. Feng, W.K.; Dun, J.W.; Yi, X.Y.; Zhang, G.Q. Deformation Analysis of WoDa village Old Landslide in Jinsha River Basin Based on SBAS-InSAR Technology. *J. Eng. Geol.* **2019**, *28*, 384–393.
25. Cascini, L.; Fornaro, G.; Peduto, D. Advanced low-and full-resolution D-InSAR map generation for slow-moving landslide analysis at different scales. *Eng. Geol.* **2010**, *112*, 29–42. [[CrossRef](#)]
26. Cigna, F.; Bateson, L.B.; Jordan, C.J.; Dashwood, C. Simulating SAR geometric distortions and predicting persistent scatterer densities for ERS-1/2 and ENVISAT C-band SAR and InSAR applications: Nationwide feasibility assessment to monitor the landmass of Great Britain with SAR imagery. *Remote Sens. Environ.* **2014**, *152*, 441–466. [[CrossRef](#)]
27. Herrera, G.; Gutierrez, F.; Garcia-Davalillo, J.C.; Guerrero, J.; Notti, D.; Galve, J.P.; Fernandez-Merodo, J.A.; Cooksley, G. Multi-sensor advanced DInSAR monitoring of very slow landslides: The Tena Valley case study (central Spanish Pyrenees). *Remote Sens. Environ.* **2013**, *128*, 31–43. [[CrossRef](#)]
28. Dai, K.R.; Zhang, L.L.; Song CLi, Z.H.; Zhuo, G.C.; Xu, Q. Quantitative Analysis of Sentinel-1 Imagery Geometric Distortion and their suitability along Sichuan-Tibet Railway. *Geomat. Inf. Sci. Wuhan Univ.* **2021**. (In Chinese) [[CrossRef](#)]
29. Xu, J.Q.; Ma, T.; Lu, Y.K.; Bai, W.M.; Zhao, S. Land Subsidence Monitoring in North Henan Plain Based on SBAS-InSAR Technology. *J. Jilin Univ. Earth Sci. Ed.* **2019**, *49*, 1182–1191. [[CrossRef](#)]
30. He, X.F.; He, M. *InSAR Earth Observation Data Processing Method and Comprehensive Measurement*; Science Press: Beijing, China, 2012.
31. Ferretti, A.; Prati, C.; Rocca, F. Permanent scatterers in SAR interferometry. *IEEE Trans. Geosci. Remote. Sens.* **2001**, *39*, 21. [[CrossRef](#)]
32. Liu, G.Q. Landslide Detection and Monitoring of Danba County Based on SBAS-InSAR. Master’s Thesis, Chang’an University, Xi’an, China, 21 July 2015.
33. Doin, M.P.; Lasserre, C.; Peltzer, G.; Cavali’e, O.; Doubre, C. Corrections of stratified tropospheric delays in SAR interferometry: Validation with global atmospheric models. *J. Appl. Geophys.* **2009**, *69*, 35–50. [[CrossRef](#)]
34. Liu, X.J.; Zhao, C.Y.; Zhang, Q.; Lu, Z.; Li, Z.H. Deformation of the Baige Landslide, Tibet, China, revealed through the integration of cross-platform ALOS/ PALSAR-1 and ALOS/PALSAR-2 SAR observations. *Geophys. Res. Lett.* **2020**, *47*, e2019GL086142. [[CrossRef](#)]
35. Liang, J.T. Study On The Early Remot Sensing Identification and Evolution Characteristics of Typical Geological Disaster in High Intensity Earthquake Zone. Master’s Thesis, Chengdu University of Technology, Chengdu, China, 12 July 2018.
36. Zuo, X.F. Study on the Influence of Active Fault on Slope Hazards in Ningqiang County. Master’s Thesis, Xi’an University of Science and Technology, Xi’an, China, 21 July 2020.